Partial Hearing Restoration after ERBB2 Induction in Deafened Adult Mice

Jingyuan Zhang [1], Daxiang Na [2], Miriam Dilts [3], Kenneth S. Henry [4], and Patricia M. White [1*]

(1) Department of Neuroscience, Ernest J. Del Monte Institute for Neuroscience, University of Rochester School of Medicine and Dentistry, Rochester, NY, USA

(2) Department of Biomedical Genetics, University of Rochester School of Medicine and Dentistry, Rochester, NY, USA

(3) Department of Biology, Brigham Young University, Provo, UT, USA

(4) Department of Otolaryngology, University of Rochester School of Medicine and Dentistry, Rochester, NY, USA

(*) Corresponding Author. Department of Neuroscience, Ernest J. Del Monte Institute for Neuroscience, University of Rochester School of Medicine and Dentistry, 601 Elmwood Avenue, Rochester, NY, 14642, USA. Email: patricia_white@urmc.rochester.edu; Voice: 585 273-2340

Conflict of interest. Drs. Zhang and White are inventors on a patent, “ERBB3 activators in hearing restoration” which is related to this work.

Abstract

Noise induced hearing loss (NIHL) affects over ten million adults in the United States, and there is no biological treatment to restore endogenous function after damage. We hypothesized that activation of signaling from ERBB2 receptors in cochlear supporting cells could mitigate NIHL damage. We used the Tet-On genetic expression system to drive a constitutively active variant of ERBB2 (CA-ERBB2) in cochlear supporting cells three days after permanent noise damage in young adult mice. Hearing thresholds were assessed with auditory brainstem response tests prior to noise damage, and hearing recovery was assessed over a three month period. We evaluated supporting cell proliferation, inner and outer hair cell (IHC and OHC) survival, synaptic preservation, and IHC cytoskeletal alterations with histological techniques. Mice harboring CA-ERBB2 capability had similar hearing thresholds to control littermates prior to and immediately after noise exposure, and incurred similar levels of permanent hearing loss. Two and three months after noise exposure, CA-ERBB2+ mice demonstrated a partial but significant reversal of NIHL threshold shifts at the lowest frequency tested, out of five frequencies (n=19 total mice, p=0.0015, ANOVA). We also observed improved IHC and OHC survival (n=7 total cochleae, $p=5 \times 10^{-5}$, Kruskal-Wallis rank sum test). There was no evidence for sustained supporting cell proliferation. Some mortality was associated with doxycycline and furosemide treatments to induce the Tet-ON system. These data suggest that ERBB2 signaling in supporting cells promotes HC repair and some functional recovery. Funded by NIH R01 DC014261, and grants from the Schmitt Foundation and UR Ventures.

Introduction.

Noise-induced hearing loss (NIHL) is a permanent sensory disability disproportionately affecting former military service personnel (1, 2). Providing services and disability benefits for individuals with NIHL costs the U.S. Veterans Association over a billion dollars each year (3). Noise exposure can increase auditory thresholds for hearing (4), potentiate tinnitus (5, 6), and exacerbate the effort of understanding speech in noise (7). Cellular correlates of noise damage include deaths of outer hair cells (OHC) and inner hair cells (IHC) (8), broken cellular structures such as stereocilia and the tunnel of Corti (9), increased inflammation (10, 11), and disrupted auditory synapses through glutamate excitotoxicity (12).

Non-mammalian vertebrates, such as birds, readily regenerate lost auditory hair cells after noise (13, 14) and drug damage (15, 16). Surviving supporting cells re-enter the cell cycle, and others trans-differentiate into *de novo* hair cells. Auditory thresholds return later, with the ability to discriminate between different sounds returning after one month (17). Avian supporting cell proliferation after drug damage requires signaling through members of the epidermal growth factor receptor (EGFR) family, including ERBB2 (18). In contrast, avian hair cell differentiation is potentiated by antagonists of BMP4 (19) and NOTCH (20) signaling. To facilitate mammalian hair cell regeneration, multiple candidate pathways are under investigation, including NOTCH (21), FGF22 (22), WNT (23), SHH (24), and IGF1 (25). IGF1 has been proposed as a factor for restoring auditory function in mammals (26). Very little is known about how damaged auditory hair cells may be repaired.

We have focused on signaling through the ERBB2 receptor as a candidate for initiating a damage response in the cochlea. In other epithelial tissues, ERBB2 signaling is activated after stretch damage (27) to promote repair and regeneration. All four members of the ERBB receptor family are expressed by mammalian supporting cells throughout life (28), and early studies implicated EGF family ligands in inner ear proliferation (29). Moreover, endogenous ERBB2 signaling in supporting cells maintains cochlear neuronal survival through a signaling cascade (30). To assess the effects of ERBB2 signaling, we have employed genetic methods to drive expression of a constitutively active variant of ERBB2 (CA-ERBB2) in supporting cells (31). This variant autodimerizes within the membrane to stimulate activation of PI3K (32), a key modulator of regeneration in avian tissues (33). In previous studies of CA-ERBB2 activation in undamaged, neonatal mouse cochleae, we found that supporting cells harboring CA-ERBB2 acted indirectly to stimulate changes in the cells around them,

including proliferation and ectopic hair cell differentiation (31). However, it is well described that the rodent cochlea becomes less responsive to regeneration signals prior to the onset of hearing (34, 35).

To test the efficacy of ERBB2 signaling in hearing restoration after noise damage, we have employed the same genetic mouse model used previously (31) in a noise damage paradigm. Young mice harboring a CA-ERBB2 transgene (32) were exposed to traumatic noise, which permanently abolishes auditory function in control mice of that age and strain (36). The mice were then subjected to pharmacological induction of the transgene in supporting cells (37). Functional and anatomical studies were conducted to assess the long-term effects of this intervention.

Results.

We hypothesized that activation of ERBB2 signaling in cochlear supporting cells after noise damage would promote hearing recovery. To test this hypothesis, we employed a genetic model of noise damage in young adult mice, taking advantage of the age-dependent sensitivity to noise documented for CBA/CaJ (38) and their F1 hybrids (39, 40). We obtained double heterozygotes harboring the *Fgfr3-iCRE* genetic modification (37) or the *Tet-ON-CA-ERBB2* transgene (32) after separately breeding both parent lines to CBA/CaJ for 5 generations (S. Fig. 1, line 1). Double heterozygotes were bred to mice homozygous for a *ROSA-flox-rtTA-IRES-GFP* modification, which had been bred to the C57BL/6J line (S. Fig. 1, line 2). From the second pairing, we obtained mice harboring all three genetic modifications ("CA-ERBB2") and littermates harboring two of the three modifications, which served as controls ("control"). After injecting tamoxifen into all mice to induce recombination of the ROSA locus, we tested their hearing at post natal day 28 (P28) by recording Auditory Brainstem Responses (ABR) to tone pips of different frequencies (Fig. 1A, "pre-test"). No differences were seen between the genotypes at all 5 frequencies (Fig. 1B, 8, 12, 16, 24 and 32 kHz, p=0.7, 10 control and 9 CA-ERBB2 mice, ANOVA).

Approximately one week after the pre-test, mice were exposed to an 8-16 kHz octave band of noise at 110 dB for two hours (Fig. 1A), which was shown to induce permanent threshold shifts in young CBA/CaJ adults (41). Significant threshold shifts were observed 1 day post noise exposure (DPN), with no differences observed between CA-ERBB2 mice and their control littermates (Fig. 1C, p=0.91, 10 control and 9 CA-ERBB2 mice, ANOVA). Two days after this hearing test, mice were fed chow laced with doxycycline (Fig. 1A, pink bar). They also received a single injection of doxycycline and EdU in combination, followed by an injection of furosemide 30 minutes later (Fig. 1A). This protocol has been shown to be effective in driving Tet-ON promoters in cochlear supporting cells (42). Effects of this intervention on ABR thresholds were assessed at 30, 60 and 90 DPN (Fig. 1A), by an independent expert blinded to both genotype and time point.

To assess hearing recovery, we calculated ABR threshold shifts for each mouse by subtracting pre-test auditory thresholds from those obtained at different times after noise exposure. Positive values indicate hearing loss. In Fig. 2, ABR shifts are plotted for the 8 kHz frequency for 10 control mice (Fig. 2A, open circles) and 9 CA-ERBB2 mice (Fig. 2A, pink circles) for the four time points after noise exposure. No differences were seen overall between the genotypes at 30 DPN (p=0.33, 10 controls, 9 CA-ERBB2 mice,

ANOVA) or in 8 kHz ABR shifts specifically (p=0.26, 10 controls, 9 CA-ERBB2 mice, two-tailed t-test with Bonferroni adjustment). In contrast, at 60 DPN, CA-ERBB2 mice displayed partial but significant reductions in their ABR shifts (p=0.0015, 10 controls, 9 CA-ERBB2 mice, ANOVA), which was due to changes in CA-ERBB2 shifts at 8 kHz (Fig. 2A, p=0.008, 10 controls, 9 CA-ERBB2 mice, two-tailed t-test with Bonferroni adjustment). This functional recovery from noise damage was sustained through 90 DPN (Fig. 2A, p=0.017, 10 controls, 9 CA-ERBB2 mice, two-tailed t-test with Bonferroni adjustment). In absolute terms, the mice recovered an average of 13.3 ± 4.6 dB, or about 41% of the threshold shift. Threshold shifts for the other four frequencies were not significantly different between genotypes (S. Fig. 2).

Representative 8 kHz ABR traces for a control mouse (Fig. 2B-E) and a CA-ERBB2 mouse (Fig. 2F-I) illustrate this hearing recovery. These mice displayed similar pre-test thresholds (Fig. 2B, cf. F) and a complete loss of hearing thresholds 1 DPN (Fig. 2C, cf. G). Hearing recovery was evident in the CA-ERBB2 mouse at 30 DPN (Fig. 2H) which continued to improve over the next two months (Fig. 2I). No such recovery was evident in the control mouse (Fig. 2E).

To assess proliferation by supporting cells, we prepared whole mount cochleae for EdU fluorescence (Fig. 3, white). Preparations were also immunostained with antibodies against GFP (Fig. 3, green), the OHC marker Oncomodulin (OCM, Fig. 3, violet), and the pan-hair cell marker Myosin7 (MYO7, Fig. 3, red). The presence of GFP indicates which cells had recombined the *ROSA-rtTA/GFP* locus and also continued to express it throughout adulthood. Representative confocal stacks for the apical region of a control (Fig. 3A-A”) and a CA-ERBB2 cochleae (Fig. 3B-B”) are shown. Both were obtained from mice euthanized at 90 DPN. GFP+ pillar cells are seen in the cross-sections (Fig 3A’, B’, white arrows), among the surviving OHC (Fig. 3A, B, purple) and IHCs (Fig. 3A, B, red). A single faint EdU+ nucleus can be seen in the CA-ERBB2 cochlea (Fig. 3B”, arrowhead), underneath the OHCs (Fig. 3B, arrowhead). The EdU+ cell is not GFP+ (Fig.3B” cf. B’). This is the only EdU+ supporting cell observed at this time point (3 whole mount cochleae and 3 sectioned cochleae). These data indicate that supporting cell proliferation was not likely a significant consequence from CA-ERBB2 activation in young adults.

To assess hair cell loss, we generated cochleograms from the same preparations used in Fig. 3. Composite representative images are shown, with anti-OCM staining (Fig. 4A, D, violet) to reveal OHCs, and anti-MYO7 (Fig. 4A, D, red) to reveal IHCs. After frequency mapping, hair cell loss was quantified in 100

micron segments and graphed as scatter plots (Fig. 4C, D). Data from 3 CA-ERBB2 mice (pink) and 4 control mice (gray) were plotted together. Basal segments in control cochleae had lost both OHCs (Fig. 4C, gray) and IHCs (Fig. 4D, gray) at 90 DPN. Notably, significantly fewer OHC losses were observed in cochleae that experienced CA-ERBB2 activation (Fig. 4C, $p = 5x10^{-5}$, 4 control cochleae, 3 CA-ERBB2 cochleae, Kruskal-Wallis rank sum test). IHC losses were also reduced in cochleae that experienced CA-ERBB2 activation (Fig. 4D, $p = 0.003$, 4 control cochleae, 3 CA-ERBB2 cochleae, Kruskal-Wallis rank sum test). OHCs in these basal regions were normally positioned in three rows above supporting cells, and few or no ectopic hair cells were observed (Fig. 4B). These data indicate that ERBB2 activation after noise damage correlates with improved hair cell survival.

We examined IHC morphology with immunostaining for MYO7, comparing age-matched, unexposed control mice with control mice at 90 DPN and CA-ERBB2 mice at 90 DPN (Fig. 5). 12 and 24 kHz regions were analyzed in order to compare with previously published results (43-45). At 12 kHz, the morphology of IHCs were indistinguishable between the groups (Fig. 5A-C, blue staining). 3D reconstructions in Amira appeared similar (Fig. 5G-I, white). At 24 kHz, noise damaged IHCs displayed an altered appearance (Fig. 5E, cf. D). Rather than a gourd-shaped morphology filled with MYO7 (Fig. 5D), noise damaged IHCs in control mice displayed large gaps or holes in MYO7 staining (Fig. 5E, arrows). Gaps were also seen in CA-ERBB2 IHCs (5F, arrow), but were not as dramatic. Gaps were still evident in 3D reconstructions of the data for both genotypes, where IHCs were rotated to present at the same viewing angle (Fig. 5K, L).

Noise damage can reduce synaptic pairing under conditions that impose large but temporary threshold shifts (44). Noise also promotes hypertrophy of high-frequency ribbons (45). We quantified synaptic pairs per IHC in Amira 3D reconstructions. The analyst was blinded to genotype, frequency, and condition. At 12 kHz, age-matched unexposed control mice, control mice at 90 DPN, and CA-ERBB2 mice at 90 DPN showed no significant differences with 12.4 ± 0.7, 14.8 ± 2.2, and 11.2 ± 1.4 synapses per IHC respectively, (mean ± s.e.m., n=3 biological replicates per condition). We plotted the ribbon sizes to assess the distributions in violin plots (Fig. 6A). Mean sizes for the three conditions were 0.24 ± 0.02, 0.24 ± 0.01, and 0.38 ± 0.02 microns^3 respectively (mean ± s.e.m., 3 biological replicates per condition). No differences were seen between control groups with or without noise exposure ($p=0.14$, n= 3 biological replicates/260-316 synapses, Kruskal-Wallis rank sum test with multiple comparison adjustment). At 90 DPN, CA-ERBB2 IHCs had significantly larger

ribbons than either control condition ($p=7x10^{-16}$ versus age matched, unexposed control synapses, $p=2x10^{-14}$ versus control mice at 90 DPN, 3 biological replicates/247-316 synapses, Kruskal-Wallis rank sum test with multiple comparison adjustment).

At 24 kHz, age-matched unexposed control mice, control mice at 90 DPN, and CA-ERBB2 mice at 90 DPN had no significant differences in synapses per IHC, (12.9 ± 2.2, 10.4 ± 1.3, and 11.3 ± 1.3 respectively, mean ± s.e.m., n=2-3 biological replicates per condition). Mean ribbon sizes for the three conditions were 0.21 ± 0.02, 0.24 ± 0.01, and 0.37 ± 0.02 microns^3 respectively (mean ± s.e.m., 2-3 biological replicates per condition). Noise exposed control IHCs had larger ribbons than age-matched unexposed control IHCs (Fig. 6B, $p=4x10^{-6}$, n= 2-3 biological replicates/164-241 synapses, Kruskal-Wallis rank sum test with multiple comparison adjustment). Noise exposed CA-ERBB2 IHCs were significantly larger than both control conditions ($p=7x10^{-16}$ versus age matched, unexposed control synapses, $p=5x10^{-13}$ versus control mice at 90 DPN, 2-3 biological replicates/164-241 synapses, Kruskal-Wallis rank sum test with multiple comparison adjustment). Taken together, we show no significant synaptic loss in this experimental system, but do suggest that after CA-ERBB2 induction, some intracellular processes within IHCs are altered in a way that leads to larger synaptic ribbon sizes.

We sought to better characterize the “gaps” in anti-MYO7 staining observed in IHCs (Fig. 5) after noise damage, using cryosections (Fig. 7). Since MYO7 is an actin-binding protein, we compared anti-MYO7 staining patterns (Fig. 7, green) to anti-MAP2, a microtubule-associated protein in the organ of Corti (46), Fig. 7, red). To outline the IHCs, we included immunostaining against GLAST/EAAT1, a glutamate transporter expressed in interphalangeal supporting cells (47), Fig. 7, magenta). We found that areas within the IHCs where anti-MYO7 staining was reduced (Fig. 7, arrows) also had reduced MAP2 immunostaining (Fig. 7, arrows), although precise co-expression was infrequent.. This suggests that gaps in anti-MYO7 staining could reflect local injury to IHC cytoskeleton. Cytoskeletal gaps were irregular in shape, and typically near the synapses, although some were observed in perinuclear regions (Fig. 7A) or between the nucleus and stereocilia (Fig. 7C). There was no obvious difference between the genotypes, suggesting that the persistence of cytoskeletal gaps is not affected by ERBB2 activation.

Discussion.

NIHL is a lifelong disability characterized in part by raised auditory thresholds and OHC loss. Here we tested the hypothesis that activating ERBB2 signaling in supporting cells after noise exposure can mitigate cochlear damage. Using a genetic expression system to drive a constitutively active ERBB2 transgene, we show that this associates with a delayed, partial recovery of hearing function in the lower frequency of young adult mice after traumatic noise exposure. High frequency OHCs and IHCs have significantly greater survival in mice with CA-ERBB2 activation. Little supporting cell proliferation is observed, and mid-frequency auditory synapses are maintained in this noise-damage paradigm. Synaptic ribbons in both 12 and 24 kHz regions are significantly hypertrophied in cochleae with induced CA-ERBB2 expression. IHC cytoskeletal damage persists in both CA-ERBB2 expressing and control cochleae. Taken together, we propose that activation of this pathway in cochlear supporting cells may promote partial hearing restoration in mammals, but does not appear to stimulate avian-like regeneration.

We observed partial but significant improvements in hearing thresholds in noise damaged mice after CA-ERBB2 induction (Fig. 2 & 3). This recovery was confined to the lowest frequency tested, 8 kHz. We also found that there are significantly more OHCs and IHCs in basal cochleae of noise-damaged mice after CA-ERBB2 induction (Fig. 4). We found no significant proliferation by cochlear supporting cells (Fig. 3). Basal OHCs and IHCs are not disorganized or ectopic (Fig. 4), and there is no evidence for supporting cell loss (not shown). Thus, we interpret the data to mean that CA-ERBB2 signaling in supporting cells promotes recovery and survival of damaged hair cells rather than the regeneration of new hair cells. In the mouse utricle, supporting cells respond to damaged hair cells by secreting HSP70, promoting their survival (48). A similar mechanism may be at work here. We note that noise damages the cochlea in a basal to apical gradient, with the greatest cellular losses in the high-frequency, basal regions. Auditory function is lost throughout most of the noise-damaged cochlea, and any residual function confined to the low-frequency, apical regions. It is promising that both low-frequency auditory function and higher-frequency hair cells survival were improved in cochleae after CA-ERBB2 expression, consistent with the interpretation that protection occurred throughout the organ. Our data also raise the possibility that damaged and dysfunctional hair cells might be repaired to restore function.

We do not find differences in the numbers of synapses on IHCs when comparing CA-ERBB2 mice exposed to noise, control littermates exposed to noise, or control littermates without noise exposure (Fig. 5). Pure CBA/CaJ mice permanently lose synapses after a noise exposure that produces a temporary hearing loss (44). Similar results were reported for FVB/nJ mice (45) and rhesus monkeys (49). In contrast, both guinea pigs (50) and C57BL6/J mice (43) have been reported to repair some damaged synapses. The results reported here suggest that in this aspect of noise damage, C57BL/6J characteristics may be dominant over those of CBA/CaJ.

We report significant ribbon hypertrophy at both low- and mid-range frequencies after noise damage and CA-ERBB2 activation (Fig. 6). Sustained hypertrophy of mid-frequency, e.g. 24 kHz, ribbons is observed in control mice after noise exposure (Fig. 6B), both with and without permanent threshold shift (45) and in multiple mouse lines (43). Hypertrophy occurs in the absence of synaptic loss, meaning that noise damage causes ribbons to grow. CTBP2 proteins exchange dynamically, but slowly, in hair cells, with a half-life in ribbon structures of around 2 hours (51). In zebra fish, the enlargement of ribbons reduces spontaneous spike rates and alters stimulus encoding latencies (52). Thus, a mechanism that maintains ribbon size likely facilitates coordinate signaling and possibly sound encoding (53). In zebra fish, reducing Ca(V)1.3 activity enlarges hair cell ribbons, and the enlargement of ribbons leads to larger calcium currents (54). These suggest that calcium currents can regulate ribbon size. To get a long-lasting enlargement of ribbons, noise damage could suppress calcium currents, or make the ribbon less sensitive to calcium by altering a putative internal IHC feedback mechanism. The second mechanism could involve modifications in levels or activities of calcium binding proteins associated with the ribbon, such as ArfGAPs (55) or otoferlin. We do not assert that ribbon hypertrophy drives hearing recovery, but we note that it likely reflects intrinsic changes in the IHC after noise damage, that could affect IHC responsiveness to stimuli. Further studies are needed to better understand synaptic maintenance and responsiveness to damage.

One major outstanding question in otolaryngology is the relative contributions of different damage correlates to hearing loss. Cochlear function requires multiple cell types to work together, including OHCs, IHCs, supporting cells, spiral ganglion neurons, efferent projections, and potassium recycling cells. We have focused attention on inner hair cells, their synapses, and their cytoskeleton (Fig. 5-7), which show clear and

persistent signs of damage. Much further work will be needed to understand which aspects of noise damage are critical for function and which ones are merely correlative.

Previous reports have shown that CA-ERBB2 can activate the downstream effector PI3K (31, 32). While it is attractive to imagine that endogenous ERBB2 activation could confer detection of stretch damage (27) in cochlear epithelium, an alternative explanation holds that transgenic CA-ERBB2 over-expression artificially activates PI3K to confer hearing restoration. Previous studies have implicated PI3K in cochlear protection from ototoxicity. Pharmacological blockade of PI3K increases outer hair cell death from gentamicin in the neonatal rat organ of Corti (56), and genetic activation of PI3K through the deletion of its inhibitor, PTEN, reduces hair cell death from cisplatin (57) or gentamicin toxicity (58). Under this interpretation, our work extends these findings in several important ways. First, we prove that activation in supporting cells alone is sufficient to promote hair cell survival, as the previous studies used either pharmacological inhibitors, deleted PTEN in both supporting cells and hair cells, or both (57, 58). Second, our work indicates that the induction of CA-ERBB2, and/or its potential effector PI3K, can rescue adult hair cells from a noise-induced death. Third, we note that we induce CA-ERBB2 three days after noise damage, indicating that there is a substantial window of time for therapeutic intervention. Lastly, the return of function to some dysfunctional hair cells suggests this signal initiates a slow process of repair. Therapies incorporating technology based on this finding could be bundled with other methods, such as those that reduce immediate damage, for combinatorial effects.

Methods.

Mice. The following mouse strains were used in these experiments. *Fgfr3-iCre* (37) was a kind gift from Dr. Jian Zuo. *CA-ErbB2* mice were purchased from Jackson Laboratories. Both lines were bred to CBA/CaJ mice (Jackson Laboratories) for five generations. *ROSA-floxed-rtTA/GFP* was a kind gift from Dr. Lin Gan. This line was made using the same modifications described by others (59) on 129SvEv and backcrossed four times to C57BL6/J (Jackson Laboratories). When crossed to an appropriate CRE-expressing line, the adult F1 cochlear supporting cells displayed GFP fluorescence (see Fig. 3). *Fgfr3-iCre* mice were crossed to *CA-ErbB2* mice, and then male mice harboring a single copy of both modifications were crossed to homozygous *ROSA-floxed-rtTA/GFP* females. Mice harboring all three modifications were designated "CA-ErbB2", and mice harboring two of the three modifications were designated "Control" throughout this article.

In all, 25 mice were prepared for this study in five separate cohorts. In the first four cohorts, 20 mice received tam injections, hearing tests, noise damage, and dox/furo injections, and 1 mouse died immediately after the dox/furo treatment. In the fifth cohort, 3/5 mice died after dox/furo injections. The surviving two mice from that cohort were not included in the results.

Both male and female mice were used equally throughout these experiments. Mice were maintained on a 12 hour light-dark cycle. No more than five adults were housed per cage with food and water available ad libitum. Mice also received ample nesting supplies and small houses. The day that pups were found was designated P0. Genotyping primers and protocols are available upon request.

Administration of substance to mice. Mice received three i.p. injections of tamoxifen (tam: 75 mg/kg, Sigma, #T5648) dissolved in corn oil (Sigma, #C8267) at 5 mg/kg, starting at P21. Injections were once a day, given over three consecutive days. Mice were fed chow laced with doxycycline (200 mg/kg of chow, BioServ #S3888), as described in the text. They also received a single i.p. injection of doxycycline hyclate (dox: 100 mg/kg body weight, Sigma Aldrich #D9891), which was freshly prepared as 10 mg/ml stock in 0.9% sterile saline, and two injections of 5-ethynyl-2´-deoxyuridine (EdU: 0.01 mg/kg, Invitrogen #A10044), made as a 10 mM stock solution in DMSO and diluted for injection to 40% strength in 0.9% sterile saline. The dox injection was followed by an injection of furosemide (furo: 400 mg/kg, Merck #21784-46150) dissolved in 0.9% sterile saline after a 30 minute interval.

Noise exposure. Awake P35 mice were exposed to noise limited to the 8-16 kHz octave band at 110 decibels (dB) for 120 minutes. Mice were each placed into individual triangular wire mesh cages, 12 cm x 5 cm x 5 cm, in an asymmetric plywood box with a JBL2250HJ compression speaker and JBL2382A biradial horn mounted on top. This apparatus was contained within a sound booth. The speaker was driven by a TDT RX6 multifunction processor and dedicated attenuator, and controlled with TDT RPvdsEx sound processing software. The sound level was calibrated with a Quest Technologies sound meter, Model 1900. Mice were randomly assigned to positions in the noise chamber using a deck of cards, and were exposed between the hours of 9 AM and 3 PM to control for circadian rhythm effects (60), and the sound level was checked with an iPhone using the FaberAcoustical SoundMeter app and the iPhone's internal microphone each morning before use. The iPhone was previously calibrated with the SoundMeter app software and the solid state 94 dB source (provided with the Quest sound meter) in a sound booth.

Auditory testing. Mice were tested on the schedule described in the text (Fig. 1A). Auditory testing was conducted using a Smart EP Universal Smart Box (Intelligent Hearing Systems). Mice were anesthetized with an intraperitoneal injection of ketamine (80 mg/kg) in a sterile acepromazine/saline mixture (3 mg/kg). A 10B+ (high frequency transducer/stimulator) probe was placed at the opening to the external auditory meatus. Auditory brainstem response (ABR) stimuli were 5-ms clicks, or 5-ms tone pips presented at 5 frequencies between 8 and 32 kHz. Stimuli began at 75 dB amplitude and decreased by 5 dB steps to 15-25 dB. 512 sweeps were averaged for each frequency and amplitude. Electrical responses were measured with three subdermal needle electrodes (Grass): one inserted beneath each pinna, and a third, the ground electrode, placed at the vertex. ABR thresholds for a particular frequency were determined by any part of the last visible trace (dB). If no waveform was observed, the threshold was noted as "80 dB." The person scoring the waveforms scored all of them at the same time. Genotype and time point were masked, and the order of the tests was randomized, using a deck of cards.

Tissue preparation for immunostaining. Cochlear organs were dissected out of freshly euthanized animals. Their stapes were removed, and a hole was made in their apical tips to allow for adequate fluid exchange.

Tissues were immersed in 4% paraformaldehyde in PBS for at least overnight. Tissues were decalcified in 0.1M EDTA at 4°C on a rotating platform for four days. For cryosectioning, tissues were immersed in 30% sucrose in PBS overnight, embedded in OCT, frozen in liquid nitrogen, and cryosectioned at 20 microns. For HC counts and synapse analysis, whole mount preparations were microdissected into turns as previously described (61), mapped using the ImageJ plug-in from Massachusetts Eye and Ear Infirmary, and immunostained.

Antibodies. The following primary antibodies were used: mouse anti-CTBP2 (aka C-Terminal Binding Protein 2; 1:200; BD Transduction Laboratories; RRID:AB_399431), chicken anti-GFP (1:500; Abcam; RRID:AB_300798), rabbit anti-GLAST (aka EAAT1; 1:100; Abcam; RRID:AB_304334), mouse anti-GRIA2 (aka GluR2/GluA2; 1:2000; Millipore; RRID:AB_2113875), mouse anti-MAP2 (aka Microtubule-Associated Protein 2; 1:250; R&D Systems, Cat #: MAB8304, RRID:AB_2814693), rabbit anti-Myosin7 (MYO7) (1:200; Proteus; RRID:AB_10013626), mouse anti-Myosin7 (1:100; Developmental Studies Hybridoma Bank, RRID:AB_2282417), and goat anti-Oncomodulin (OCM) antibody (1:1000; Santa Cruz; RRID:AB_2267583). The following secondary antibodies, all purchased from Jackson ImmunoResearch, were used: Donkey anti-Chicken 488 (1:500; RRID:AB_2340376), Donkey Anti-Mouse 488 (1:500; RRID:AB_2340849), Donkey Anti-Rabbit 594 (1:500; RRID:AB_2340622), Donkey Anti-Rabbit 647 (1:200; RRID:AB_2340625), Donkey Anti-Goat 647 (1:200; RRID:AB_2340438), Alexa 594 Goat Anti-Mouse (IgG1, 1:500; RRID:AB_2338885), Alexa 488 Goat Anti-Mouse (IgG2a, 1:500; RRID:AB_2338855), Alexa 594 Goat Anti-Mouse (IgG3, 1:500; RRID: AB_2632543), Alexa 488 Goat Anti-Mouse (IgG1, 1:500; RRID: AB_2632534).

Immunostaining. For immunostaining on mouse sections, blocking was carried out at room temperature for two hours in 1% Tween / 5% goat serum (Jackson) in Tris-buffered saline. Antibody incubations were carried out overnight at 4°C in block solution. For whole mount staining, dissected mapped turns were flash frozen in liquid nitrogen, allowed to thaw, and washed in room temperature Dulbecco's PBS (Gibco). To reveal EdU incorporation, the Click-IT reaction was performed according to the manufacturer's instructions. Prior to immunostaining, tissues were blocked for one hour in 1% Triton / 5% donkey serum in PBS. Primary antibody incubations of anti-MYO7, anti-OCM, anti-GFP, anti-CTBP2, and anti-GRIA2 were performed at 37°C for 20

hours. The tissue was washed in PBS, and secondary antibody incubation was performed at 37°C for an additional 2 hours. All tissue was mounted using ProLong Gold (Fisher). Whole mounts were placed between two 50 mm coverslips for imaging.

Confocal microscopy and image processing for figures. Imaging was performed on an Olympus FV1000 or a Nikon A1R HD, both laser scanning confocal microscopes. ImageJ (NIH) was used to Z-project maximal brightness in confocal stacks, select optical sections, and combine colors. Photoshop CS5 (Adobe) was used to set maximal and background levels of projections for the construction of figures. Composite images for cochleograms were assembled in Photoshop by pasting each optical section into its own layer, and merging the pieces of the optical sections where HCs were evident. Alternatively, projections of confocal stacks were used when individual IHCs could be clearly distinguished. Composite or projected images for the mapped regions of each organ were assembled in a single file in Photoshop. 100 micron lengths were pasted onto the images on the row of pillar cells, and OHCs were counted to determine the percent lost. Where the loss of OHCs was great enough (>30%), an average OHC count, determined from low-frequency regions of the same cochlea, was used as the denominator.

3-D reconstructions of synaptic components. To quantitatively assess synaptic number and distribution in IHCs, we used immunofluorescence and confocal microscopy in conjunction with three-dimensional modeling. Anti-CTBP2 labeled IHC nuclei and pre-synaptic ribbon structures (62), and anti-GRIA2 was specific for the post-synaptic AMPA receptor (63). Anti-MYO7 labeled IHCs (64). The most effective imaging of ribbon synaptic complexes had illumination bathing the neurites, with light collection from the stereocilliary side. Confocal data files (.oib) of appropriately stained IHCs, imaged at 200X on the FV1000, were obtained for the entire dataset, and then the files were blinded and randomized using a deck of cards. We imported the data into Amira 6.0 (Visualization Science Group) to generate 3-D reconstructions.

A Myo7a isosurface was created from the data, appropriately thresholded, and exported. The CTBP2 and GRIA2 datasets were subjected to blind deconvolution, performed using the “maximum likelihood estimation” package for Amira. Briefly, point spread functions used for deconvolution were calculated using the optical parameters of the microscope (N.A. =1.40, UPlanSAPO 100x oil objective, 400-800 nm) and the

wavelength of interest, and the datasets were deconvolved for 5 iterations. The data were despeckled, and then isosurfaces were created from the data and appropriately thresholded. The Connected Components function was used to output a complete list of all CTBP2 structures. To identify pairs of synaptic components, we used the Amira XImagePAQ AND functionality, which identifies adjacent staining elements. Those elements were dilated and subtracted from the CTBP2 dataset to identify "orphan" or unpaired synaptic ribbons. The complete list and the "orphan" list were compared to obtain paired ribbons. Only after synaptic pairs were processed was the MYO7 data visualized for display.

Statistics. Statistical analyses were performed in R. Datasets that failed the Shapiro-Wilk normality test were analyzed with the Kruskal-Wallis rank sum test; otherwise, we performed a multivariable ANOVA. Subsequent pairwise analysis was performed using the Bonferroni adjustment for multiple comparisons.

Data availability. All primary data were reviewed by the senior author prior to the assembly of figures for this paper. Any differences between the data presented here and any other public presentation are due to errors that were caught in that review. All the original data are available upon request to the senior author.

Study approval. The University Committee for Animal Resources (UCAR) reviewed and approved these mouse experiments prior to their initiation.

Author Contributions.

JZ and PW conceived, planned, and performed experiments, and analyzed data. DN and MD performed experiments and analyzed data. KH analyzed masked and randomized ABR data as the independent expert. PW wrote the paper.

Acknowledgements.

We gratefully acknowledge Dr. Anne Luebke, who maintains the URMC Small Animal Auditory Testing Core; Dr. V. Kaye Thomas, who maintains the URMC Center for Advanced Light Microscopy and Nanoscopy; Dr. Jian Zuo for the *Fgfr3*-iCre mouse strain; Dr. Lin Gan for the ROSA-floxed rtTA/GFP mouse strain; Ms. Lisa Shah, for technical assistance; and Ms. Holly Beaulac, for critically reading the manuscript.

References.

1. Humes LE, Joellenbeck LM, and Durch JS. *Noise and Military Service: Implications for Hearing Loss and Tinnitus.* Washington, D.C.: Institute of Medicine; 2006.
2. Pearson C. *A Modern Approach to Noise-induced Hearing Loss from Military Operations*. Deafness Research UK, London; 2009.
3. Annual-Benefit-Report. In: Administration V ed.: Dept. of Veterans Affairs Veterans Benefits Administration; 2014.
4. NIDCD. Noise Induced Hearing Loss. https://www.nidcd.nih.gov/health/noise-induced-hearing-loss. Updated May 31, 2019, 2019.
5. Eggermont JJ, and Roberts LE. The neuroscience of tinnitus. *Trends in neurosciences.* 2004;27(11):676-82.
6. Yankaskas K. Prelude: noise-induced tinnitus and hearing loss in the military. *Hear Res.* 2013;295(3-8.
7. Hygge S, Evans GW, and Bullinger M. A prospective study of some effects of aircraft noise on cognitive performance in schoolchildren. *Psychol Sci.* 2002;13(5):469-74.
8. Chen GD, and Fechter LD. The relationship between noise-induced hearing loss and hair cell loss in rats. *Hear Res.* 2003;177(1-2):81-90.
9. Lim DJ, and Dunn DE. Anatomic correlates of noise induced hearing loss. *Otolaryngologic clinics of North America.* 1979;12(3):493-513.
10. Fujioka M, Kanzaki S, Okano HJ, Masuda M, Ogawa K, and Okano H. Proinflammatory cytokines expression in noise-induced damaged cochlea. *J Neurosci Res.* 2006;83(4):575-83.
11. Hirose K, and Liberman MC. Lateral wall histopathology and endocochlear potential in the noise-damaged mouse cochlea. *J Assoc Res Otolaryngol.* 2003;4(3):339-52.
12. Puel JL, Ruel J, Gervais d'Aldin C, and Pujol R. Excitotoxicity and repair of cochlear synapses after noise-trauma induced hearing loss. *Neuroreport.* 1998;9(9):2109-14.
13. Corwin JT, and Cotanche DA. Regeneration of sensory hair cells after acoustic trauma. *Science.* 1988;240(4860):1772-4.
14. Ryals BM, and Rubel EW. Hair cell regeneration after acoustic trauma in adult Coturnix quail. *Science.* 1988;240(4860):1774-6.
15. Tucci DL, and Rubel EW. Physiologic status of regenerated hair cells in the avian inner ear following aminoglycoside ototoxicity. *Otolaryngol Head Neck Surg.* 1990;103(3):443-50.
16. Lippe WR, Westbrook EW, and Ryals BM. Hair cell regeneration in the chicken cochlea following aminoglycoside toxicity. *Hear Res.* 1991;56(1-2):203-10.
17. Ryals BM, Dent ML, and Dooling RJ. Return of function after hair cell regeneration. *Hear Res.* 2013;297(113-20.
18. White PM, Stone JS, Groves AK, and Segil N. EGFR signaling is required for regenerative proliferation in the cochlea: conservation in birds and mammals. *Dev Biol.* 2012;363(1):191-200.
19. Lewis RM, Keller JJ, Wan L, and Stone JS. Bone morphogenetic protein 4 antagonizes hair cell regeneration in the avian auditory epithelium. *Hear Res.* 2018;364(1-11.
20. Daudet N, Gibson R, Shang J, Bernard A, Lewis J, and Stone J. Notch regulation of progenitor cell behavior in quiescent and regenerating auditory epithelium of mature birds. *Dev Biol.* 2009;326(1):86-100.
21. Mizutari K, Fujioka M, Hosoya M, Bramhall N, Okano HJ, Okano H, and Edge AS. Notch inhibition induces cochlear hair cell regeneration and recovery of hearing after acoustic trauma. *Neuron.* 2013;77(1):58-69.
22. Li S, Hang L, and Ma Y. FGF22 protects hearing function from gentamycin ototoxicity by maintaining ribbon synapse number. *Hear Res.* 2016;332(39-45.
23. Shi F, Cheng YF, Wang XL, and Edge AS. Beta-catenin up-regulates Atoh1 expression in neural progenitor cells by interaction with an Atoh1 3' enhancer. *J Biol Chem.* 2010;285(1):392-400.
24. Lu N, Chen Y, Wang Z, Chen G, Lin Q, Chen ZY, and Li H. Sonic hedgehog initiates cochlear hair cell regeneration through downregulation of retinoblastoma protein. *Biochem Biophys Res Commun.* 2013;430(2):700-5.
25. Yamahara K, Yamamoto N, Nakagawa T, and Ito J. Insulin-like growth factor 1: A novel treatment for the protection or regeneration of cochlear hair cells. *Hear Res.* 2015;330(Pt A):2-9.

26. Yamahara K, Nishimura K, Ogita H, Ito J, Nakagawa T, Furuta I, Kita T, Omori K, and Yamamoto N. Hearing preservation at low frequencies by insulin-like growth factor 1 in a guinea pig model of cochlear implantation. *Hear Res.* 2018;368(92-108.
27. Vermeer PD, Einwalter LA, Moninger TO, Rokhlina T, Kern JA, Zabner J, and Welsh MJ. Segregation of receptor and ligand regulates activation of epithelial growth factor receptor. *Nature.* 2003;422(6929):322-6.
28. Hume CR, Kirkegaard M, and Oesterle EC. ErbB expression: the mouse inner ear and maturation of the mitogenic response to heregulin. *J Assoc Res Otolaryngol.* 2003;4(3):422-43.
29. Yamashita H, and Oesterle EC. Induction of cell proliferation in mammalian inner-ear sensory epithelia by transforming growth factor alpha and epidermal growth factor. *Proc Natl Acad Sci U S A.* 1995;92(8):3152-5.
30. Stankovic K, Rio C, Xia A, Sugawara M, Adams JC, Liberman MC, and Corfas G. Survival of adult spiral ganglion neurons requires erbB receptor signaling in the inner ear. *J Neurosci.* 2004;24(40):8651-61.
31. Zhang J, Wang Q, Abdul-Aziz D, Mattiacio J, Edge AS, and White PM. ERBB2 signaling drives supporting cell proliferation in vitro and apparent supernumerary hair cell formation in vivo in the neonatal mouse cochlea. *Eur J Neurosci.* 2018;48(10):3299.
32. Xie W, Chow LT, Paterson AJ, Chin E, and Kudlow JE. Conditional expression of the ErbB2 oncogene elicits reversible hyperplasia in stratified epithelia and up-regulation of TGFalpha expression in transgenic mice. *Oncogene.* 1999;18(24):3593-607.
33. Montcouquiol M, and Corwin JT. Intracellular signals that control cell proliferation in mammalian balance epithelia: key roles for phosphatidylinositol-3 kinase, mammalian target of rapamycin, and S6 kinases in preference to calcium, protein kinase C, and mitogen-activated protein kinase. *J Neurosci.* 2001;21(2):570-80.
34. Maass JC, Gu R, Basch ML, Waldhaus J, Lopez EM, Xia A, Oghalai JS, Heller S, and Groves AK. Changes in the regulation of the Notch signaling pathway are temporally correlated with regenerative failure in the mouse cochlea. *Frontiers in cellular neuroscience.* 2015;9(110.
35. Maass JC, Gu R, Cai T, Wan YW, Cantellano SC, Asprer JS, Zhang H, Jen HI, Edlund RK, Liu Z, et al. Transcriptomic Analysis of Mouse Cochlear Supporting Cell Maturation Reveals Large-Scale Changes in Notch Responsiveness Prior to the Onset of Hearing. *PLoS One.* 2016;11(12):e0167286.
36. Myint A, White CH, Ohmen JD, Li X, Wang J, Lavinsky J, Salehi P, Crow AL, Ohyama T, and Friedman RA. Large-scale phenotyping of noise-induced hearing loss in 100 strains of mice. *Hear Res.* 2016;332(113-20.
37. Cox BC, Liu Z, Lagarde MM, and Zuo J. Conditional gene expression in the mouse inner ear using Cre-loxP. *J Assoc Res Otolaryngol.* 2012;13(3):295-322.
38. Henry KR. Noise and the young mouse: genotype modifies the sensitive period for effects on cochlear physiology and audiogenic seizures. *Behavioral neuroscience.* 1984;98(6):1073-82.
39. Milon B, Mitra S, Song Y, Margulies Z, Casserly R, Drake V, Mong JA, Depireux DA, and Hertzano R. The impact of biological sex on the response to noise and otoprotective therapies against acoustic injury in mice. *Biol Sex Differ.* 2018;9(1):12.
40. Erway LC, Shiau YW, Davis RR, and Krieg EF. Genetics of age-related hearing loss in mice. III. Susceptibility of inbred and F1 hybrid strains to noise-induced hearing loss. *Hear Res.* 1996;93(1-2):181-7.
41. Ohlemiller KK, Wright JS, and Heidbreder AF. Vulnerability to noise-induced hearing loss in 'middle-aged' and young adult mice: a dose-response approach in CBA, C57BL, and BALB inbred strains. *Hear Res.* 2000;149(1-2):239-47.
42. Walters BJ, and Zuo J. A Sox10(rtTA/+) Mouse Line Allows for Inducible Gene Expression in the Auditory and Balance Organs of the Inner Ear. *J Assoc Res Otolaryngol.* 2015;16(3):331-45.
43. Kim KX, Payne S, Yang-Hood A, Li SZ, Davis B, Carlquist J, B VG, Gantz JA, Kallogjeri D, Fitzpatrick JAJ, et al. Vesicular Glutamatergic Transmission in Noise-Induced Loss and Repair of Cochlear Ribbon Synapses. *J Neurosci.* 2019;39(23):4434-47.
44. Kujawa SG, and Liberman MC. Adding Insult to Injury: Cochlear Nerve Degeneration after “Temporary” Noise-Induced Hearing Loss. *J Neurosci.* 2009;29(14077-85.

45. Paquette ST, Gilels F, and White PM. Noise exposure modulates cochlear inner hair cell ribbon volumes, correlating with changes in auditory measures in the FVB/nJ mouse. *Scientific reports.* 2016;6(25056.
46. Oshima T, Okabe S, and Hirokawa N. Immunocytochemical localization of 205 kDa microtubule-associated protein (205 kDa MAP) in the guinea pig organ of Corti. *Brain Res.* 1992;590(1-2):53-65.
47. Chen Z, Kujawa SG, and Sewell WF. Functional roles of high-affinity glutamate transporters in cochlear afferent synaptic transmission in the mouse. *Journal of neurophysiology.* 2010;103(5):2581-6.
48. May LA, Kramarenko, II, Brandon CS, Voelkel-Johnson C, Roy S, Truong K, Francis SP, Monzack EL, Lee FS, and Cunningham LL. Inner ear supporting cells protect hair cells by secreting HSP70. *J Clin Invest.* 2013;123(8):3577-87.
49. Valero MD, Burton JA, Hauser SN, Hackett TA, Ramachandran R, and Liberman MC. Noise-induced cochlear synaptopathy in rhesus monkeys (Macaca mulatta). *Hear Res.* 2017;353(213-23.
50. Liu L, Wang H, Shi L, Almuklass A, He T, Aiken S, Bance M, Yin S, and Wang J. Silent damage of noise on cochlear afferent innervation in guinea pigs and the impact on temporal processing. *PLoS One.* 2012;7(11):e49550.
51. Chen Z, Chou SW, and McDermott BM, Jr. Ribeye protein is intrinsically dynamic but is stabilized in the context of the ribbon synapse. *J Physiol.* 2018;596(3):409-21.
52. Sheets L, He XJ, Olt J, Schreck M, Petralia RS, Wang YX, Zhang Q, Beirl A, Nicolson T, Marcotti W, et al. Enlargement of Ribbons in Zebrafish Hair Cells Increases Calcium Currents But Disrupts Afferent Spontaneous Activity and Timing of Stimulus Onset. *J Neurosci.* 2017;37(26):6299-313.
53. Carney LH. Supra-Threshold Hearing and Fluctuation Profiles: Implications for Sensorineural and Hidden Hearing Loss. *J Assoc Res Otolaryngol.* 2018;19(4):331-52.
54. Sheets L, Kindt KS, and Nicolson T. Presynaptic CaV1.3 channels regulate synaptic ribbon size and are required for synaptic maintenance in sensory hair cells. *J Neurosci.* 2012;32(48):17273-86.
55. Dembla M, Wahl S, Katiyar R, and Schmitz F. ArfGAP3 is a component of the photoreceptor synaptic ribbon complex and forms an NAD(H)-regulated, redox-sensitive complex with RIBEYE that is important for endocytosis. *J Neurosci.* 2014;34(15):5245-60.
56. Chung WH, Pak K, Lin B, Webster N, and Ryan AF. A PI3K pathway mediates hair cell survival and opposes gentamicin toxicity in neonatal rat organ of Corti. *J Assoc Res Otolaryngol.* 2006;7(4):373-82.
57. Jadali A, Ying YM, and Kwan KY. Activation of CHK1 in Supporting Cells Indirectly Promotes Hair Cell Survival. *Frontiers in cellular neuroscience.* 2017;11(137.
58. Jadali A, and Kwan KY. Activation of PI3K signaling prevents aminoglycoside-induced hair cell death in the murine cochlea. *Biol Open.* 2016;5(6):698-708.
59. Belteki G, Haigh J, Kabacs N, Haigh K, Sison K, Costantini F, Whitsett J, Quaggin SE, and Nagy A. Conditional and inducible transgene expression in mice through the combinatorial use of Cre-mediated recombination and tetracycline induction. *Nucleic Acids Res.* 2005;33(5):e51.
60. Meltser I, Cederroth CR, Basinou V, Savelyev S, Lundkvist GS, and Canlon B. TrkB-mediated protection against circadian sensitivity to noise trauma in the murine cochlea. *Current biology : CB.* 2014;24(6):658-63.
61. Montgomery SC, and Cox BC. Whole Mount Dissection and Immunofluorescence of the Adult Mouse Cochlea. *Journal of visualized experiments : JoVE.* 2016107).
62. Schmitz F, Konigstorfer A, and Sudhof TC. RIBEYE, a component of synaptic ribbons: a protein's journey through evolution provides insight into synaptic ribbon function. *Neuron.* 2000;28(3):857-72.
63. Usami S, Matsubara A, Fujita S, Shinkawa H, and Hayashi M. NMDA (NMDAR1) and AMPA-type (GluR2/3) receptor subunits are expressed in the inner ear. *Neuroreport.* 1995;6(8):1161-4.
64. Hasson T, Heintzelman MB, Santos-Sacchi J, Corey DP, and Mooseker MS. Expression in cochlea and retina of myosin VIIa, the gene product defective in Usher syndrome type 1B. *Proc Natl Acad Sci U S A.* 1995;92(21):9815-9.

Figures.

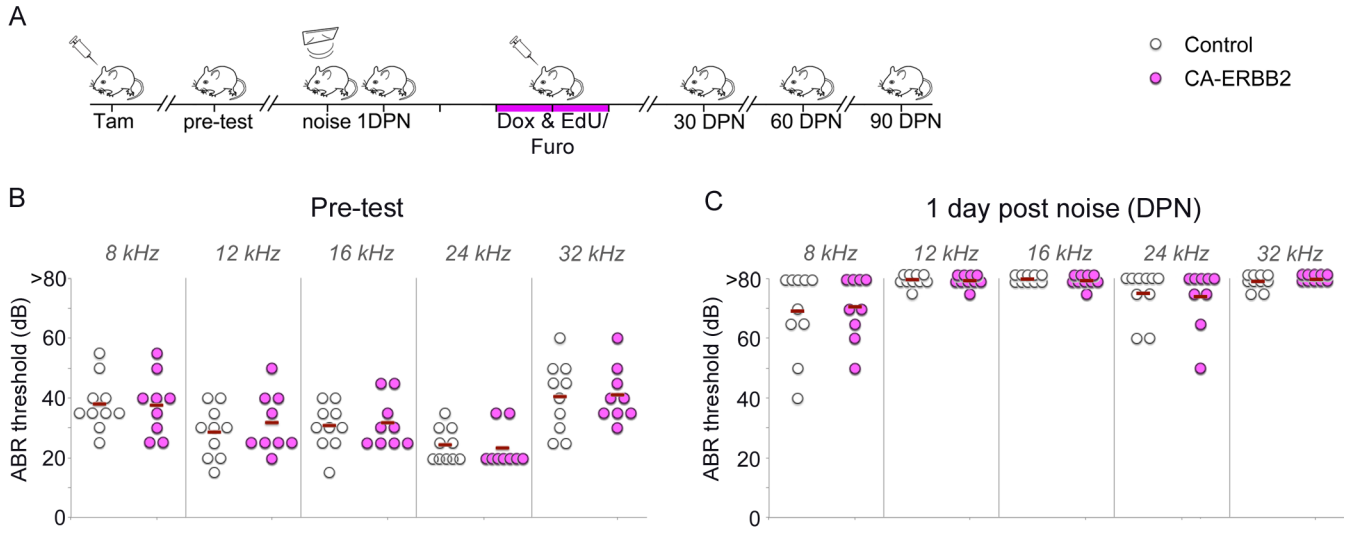

Figure 1. ABR threshold shifts after noise damage.

A. Schematic of experimental manipulations. Injections are indicated by syringes and noise exposure by a speaker. ABR hearing tests were performed prior to noise exposure (pre-test), 1 day post noise (DPN), 30 DPN, 60 DPN and 90 DPN. Tam: tamoxifen; Dox: doxycycline; EdU: ethynyl deoxyuridine; Furo: furosemide. The two day span marked with a purple bar represents dox feeding in addition to the injection.

B. ABR thresholds (in dB) are plotted for 10 control (open circle) and 9 CA-ERBB2 (pink circle) mice prior to noise exposure. Means are indicated by red bars. Five frequencies were tested. Two-way ANOVA indicates no differences between genotypes (p=0.7).

C. ABR thresholds for the same mice at the same frequencies 1 DPN. If no waveform was detected, the threshold was marked as “80 dB.” Two-way ANOVA indicates no differences between genotypes (p=0.91).

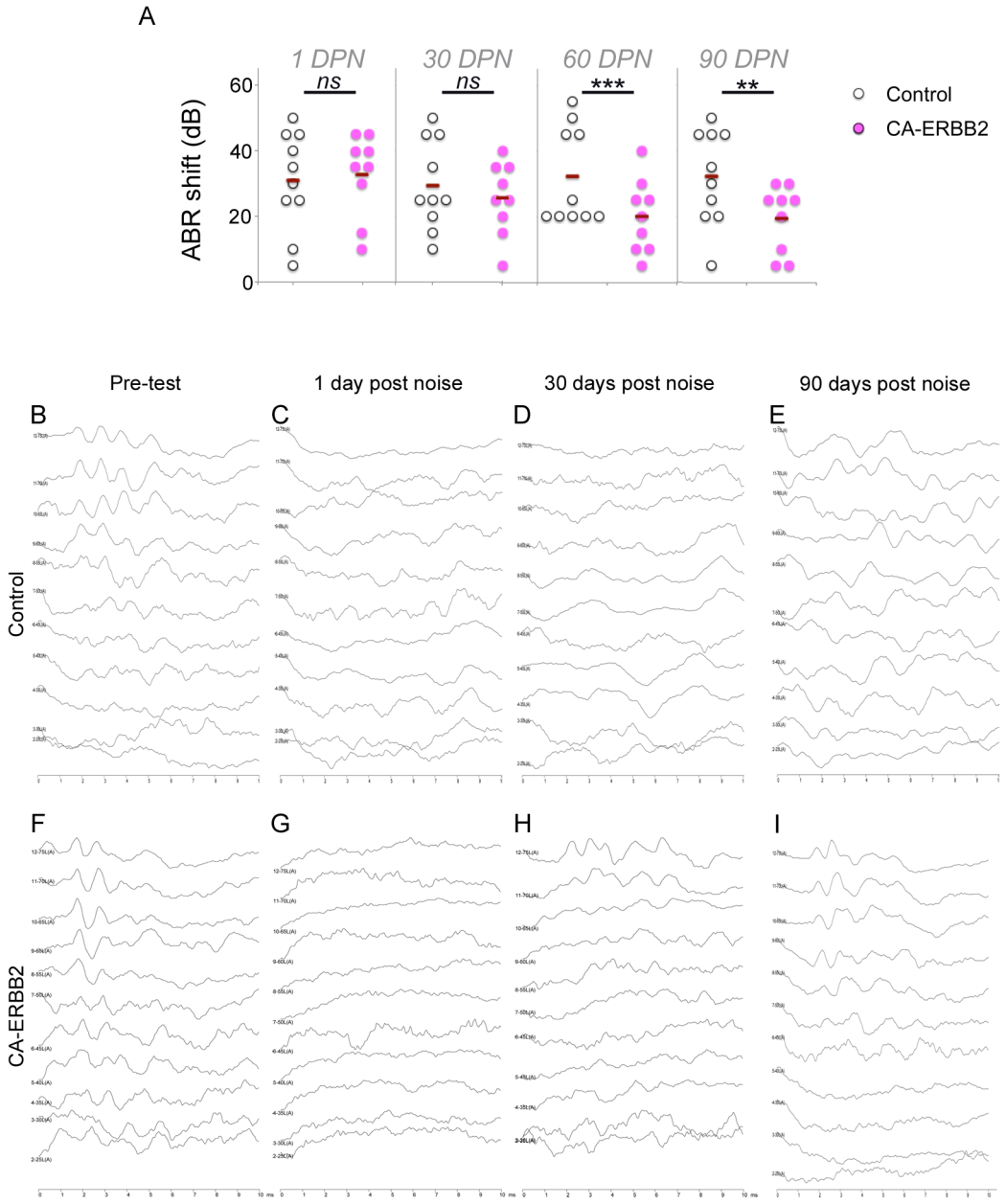

Figure 2. Partial, delayed recovery observed in CA-ERBB2 mice at 8 kHz.

A. ABR shifts (dB) were calculated for each mouse by subtracting original ABR thresholds from those obtained at different times after noise exposure. Positive values indicate hearing loss. ABR shifts from 10 control mice (open circles) and 9 CA-ERBB2 mice (pink circles) are plotted along with means for each group (red bars). ABR shifts at 30 days were not significantly different between genotypes (ANOVA p=0.34). Significant recovery was seen in the CA-ERBB2 group at 60 and 90 days (ANOVA p=0.0015, 0.017, respectively), but only for 8 kHz (Bonferroni-adjusted two tailed t-tests p=0.008, 0.013, respectively).

B-E. 8 kHz ABR traces for a representative control mouse are arranged in descending amplitudes of 5 dB steps, starting at 75 and ending at 25 dB. These include one taken before noise damage (B, Pre-test), 1 DPN (C), 30 DPN (D), and 90 DPN (E). No ABR waveforms are observed any time after noise damage.

F-I. 8 kHz ABR traces from a representative CA-ERBB2 mouse with partial recovery at the same time points. Significant improvement is observed between 30 and 90 DPN.

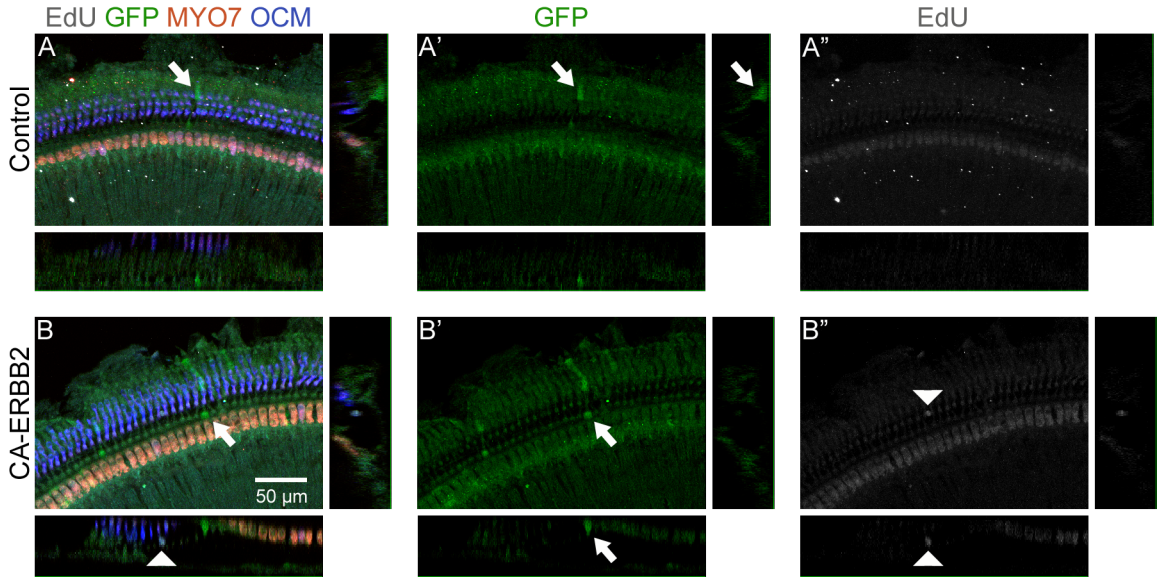

Figure 3. No significant supporting cell proliferation is observed in mice after CA-ERBB2 activation.

A. Apical segment from a representative control cochlea from 90 DPN, with immunostaining against OCM (violet) to reveal OHCs, MYO7 (red) to reveal IHCs, GFP (green) to reveal cells that recombined the *floxed-ROSA-rtTA/GFP* locus, and EdU (white) to reveal cells that had divided after treatment. Side views show *yz* projections from the confocal stack. An arrow indicates a GFP+ cell, which is an outer pillar cell in the left side view (A'). No EdU incorporation (white) is seen in the sensory epithelium (A").

B. Apical segment from a representative CA-ERBB2 cochlea, also from 90 DPN, same immunostaining as A. White arrow indicates a GFP+ supporting cell, which is adjacent to the IHC (Figure B, B', bottom side view). Note a single, faint EdU+ nucleus under the OHC layer (B, B", arrowhead). This was the only EdU+ cell observed at 90 DPN (n=3 whole mounts and 3 sectioned cochlea).

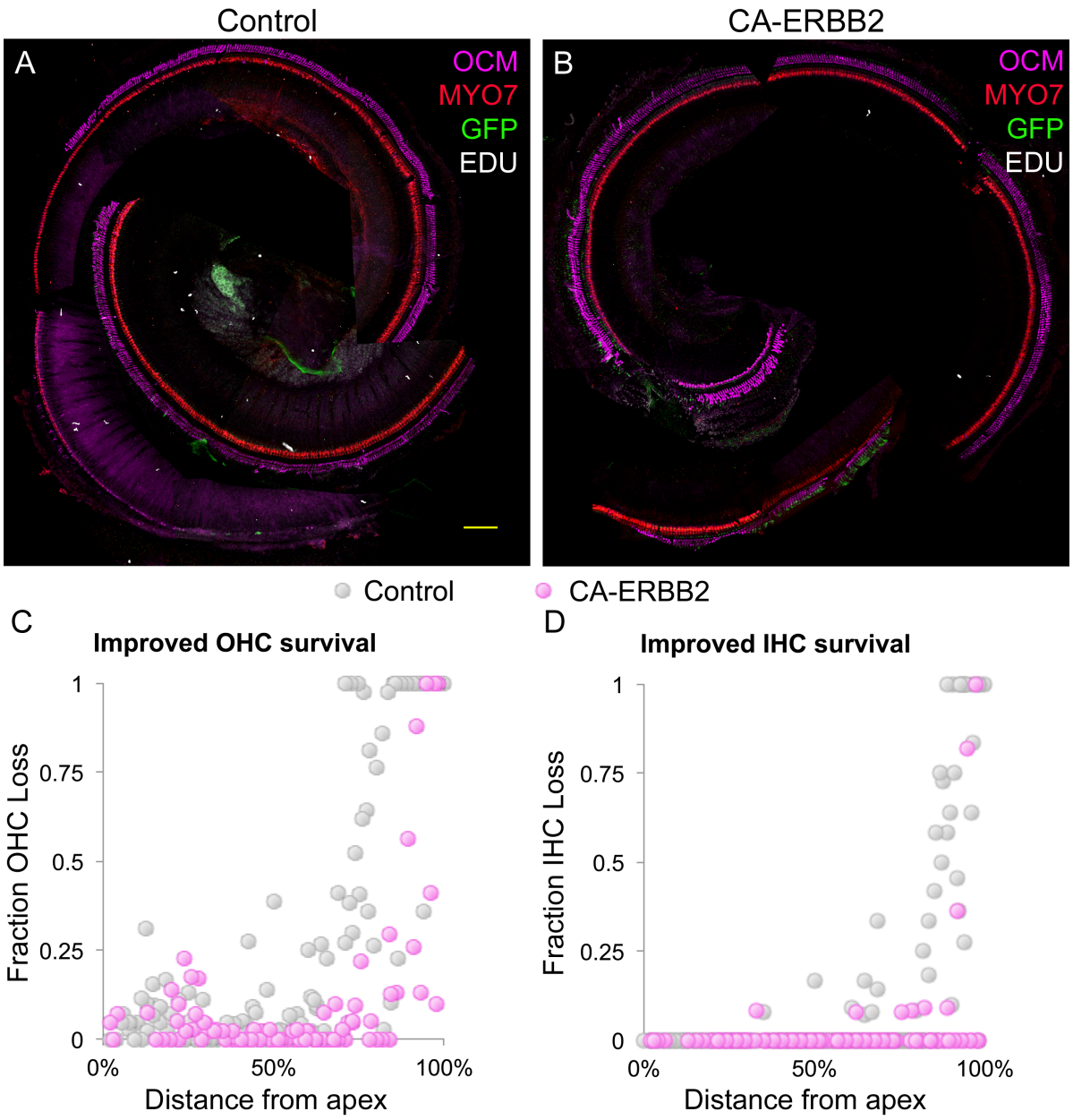

Figure 4. CA-ERBB2 induction correlates with improved OHC and IHC survival at higher frequencies.

A. Representative control cochlea from 90 DPN, with immunostaining against OCM (magenta) to reveal OHCs, MYO7 (red) to reveal IHCs, GFP (green) to reveal cells that recombined the *floxed-ROSA-rtTA/GFP* locus, and EdU (white) to reveal cells that had divided immediately after treatment. HC losses are evident in the basal segment.

B. Representative CA-ERBB2 cochlea, also from 90 DPN, same immunostaining as A. Note the HC-specific staining throughout the basal region.

C. OHC cochleogram results from control mice (gray) and CA-ERBB2 mice (pink), all at 90 DPN. OHC losses were quantified in 100 micron segments along the length of each mapped organ. OHC loss is reduced in CA-

ERBB2 cochlea compared to control cochleae ($p = 5 \times 10^{-5}$, 4 control cochleae and 3 CA-ERBB2 cochleae, both at 90 DPN, Kruskal-Wallis rank sum test).

D. IHC cochleogram results from control mice (gray) and CA-ERBB2 mice (pink), all at 90 DPN. IHC loss is reduced in comparison to control cochleae ($p = 0.003$, 4 control cochleae and 3 CA-ERBB2 cochleae, both at 90 DPN, Kruskal-Wallis rank sum test).

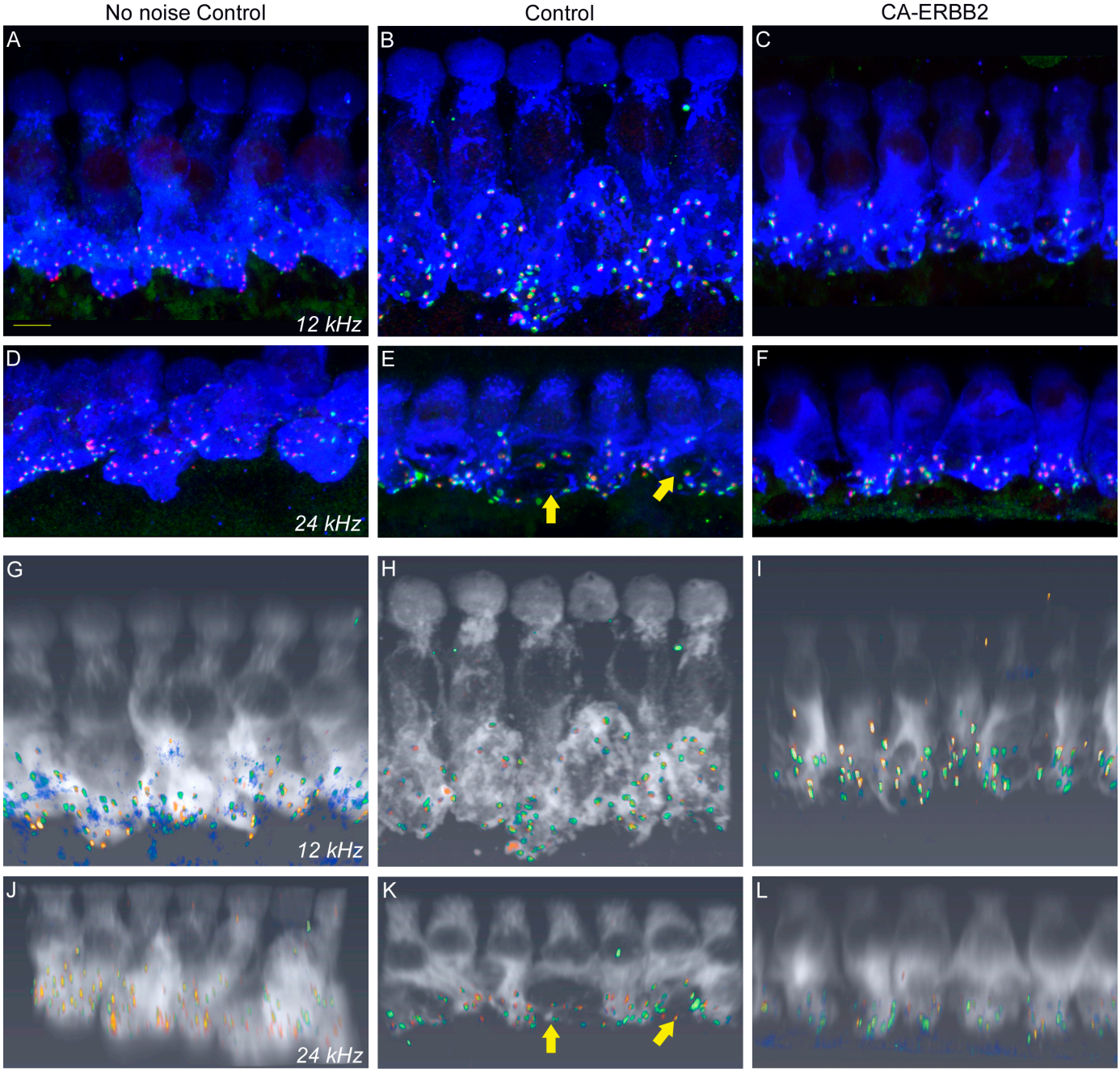

Figure 5. Representative IHC confocal images and Amira 3D reconstructions display synaptic labeling.

A-C. Representative 200x confocal images of 12 kHz IHCs from an age-matched, control mouse without noise exposure (A), a control mouse at 90 DPN (B), and a CA-ERBB2 mouse at 90 DPN. Immunolabeling for CTBP2 (red), GRIA2 (green) reveal paired synaptic structures, and immunolabeling for MYO7 (blue) reveals IHC morphology. Size bar: 5 microns.

D-F. Similar 200x confocal images of IHCs from the 24 kHz region, also from an age-matched, control mouse without noise exposure (D), a control mouse at 90 DPN (E), and a CA-ERBB2 mouse at 90 DPN (F). Arrows indicate IHCs with gaps in their MYO7 staining (E, F).

G-I. Amira 3-dimensional reconstructions from the same stacks shown in (A-C). Strong labeling for GRIA2 is coded green, while weak labeling is in blue. CTBP2 (red) and MYO7 (white) are also shown.

J-L. Amira 3-dimensional reconstructions from the same stacks shown in (D-F). IHCs were rotated to be viewed from the same approximate angle.

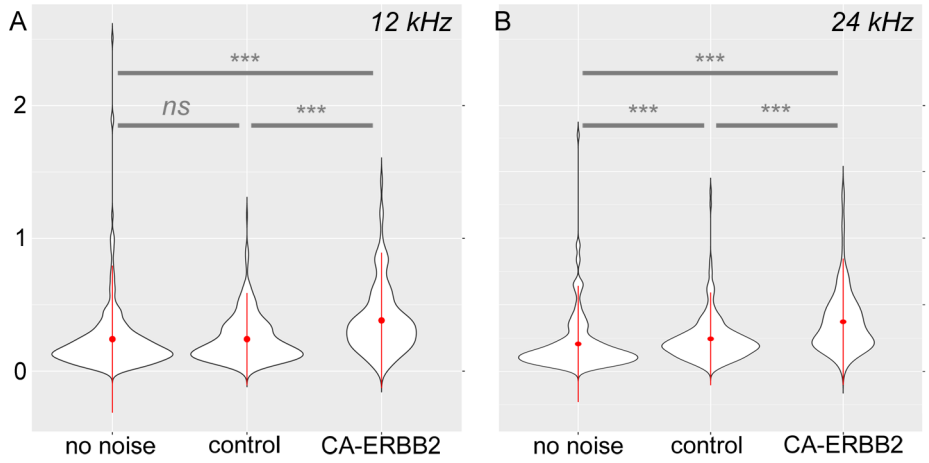

Figure 6. Significant differences in the synaptic ribbon size distribution is observed after CA-ERBB2 activation.

A. For 12 kHz IHCs, CTBP2+ ribbons were paired with GRIA2+ post-synaptic densities in Amira 3D reconstructions as described in the text. Data from age-matched control mice without noise exposure ("no noise") are compared to data from control mice at 90 DPN ("control") and data from CA-ERBB2 mice at 90 DPN ("CA-ERBB2"). Approximately 240 ribbons were identified for each condition, from 6-8 IHCs per biological replicate (3 replicates each). The size distributions of paired ribbons from each condition were plotted in violin graphs. Means are represented by a red dot and standard deviations by a red bar. Shapiro-Wilk normality tests revealed the data distribution to be non-normal. The size distribution of ribbons in control mice 90 DPN is not significantly different from similar mice without noise exposure (p=0.138, Kruskal-Wallis rank sum test with multiple comparison adjustment), whereas synapses in CA-ERBB2 mice 90 DPN differ from both control mice without noise exposure and control mice at 90 DPN ($p=6.6 \times 10^{-16}$, 2.1×10^{-14}, respectively, Kruskal-Wallis rank sum test with multiple comparison adjustment).

B. Synaptic size distributions for 24 kHz IHCs were obtained, similarly to those at 12 kHz, and plotted in violin graphs, with means represented by a red dot and standard deviations by a red bar. Data from age-matched control mice without noise exposure ("no noise") are compared to data from control mice at 90 DPN ("control") and data from CA-ERBB2 mice at 90 DPN ("CA-ERBB2"). Each distribution is significantly different each other: "no noise" vs. "control", $p=3.8 \times 10^{-6}$, "no noise" vs. "CA-ERBB2", $p=6.6 \times 10^{-16}$, and "control" vs. "CA-ERBB2", 5.2×10^{-13}. All tests, Kruskal-Wallis rank sum test with multiple comparison adjustment, 2-3 biological replicates per condition with 6-8 IHCs per replicate.

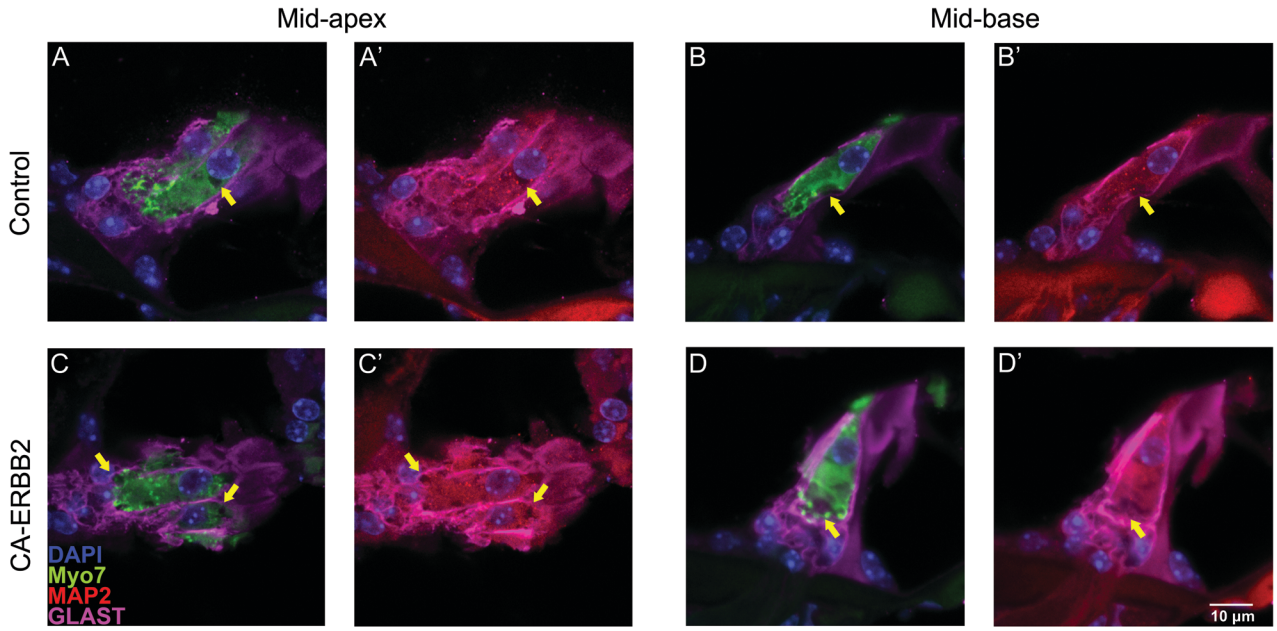

Figure 7. Loss of MYO7 immunoreactivity in IHC bodies may reflect damage to the cytoskeleton.

A, A'. A single optical section through the center of a cryosection of a IHC immunostained against MYO7 (A, green), MAP2 (A', red), GLAST (A, A', magenta) and costained with DAPI (A, A', blue). The IHC is from the mid-apical region of a control mouse cochlea obtained at 90 DPN. A staining "gap" is highlighted next to the nucleus (arrow).

B, B'. An optical section from the center of a similarly stained IHC, from the mid-basal region of a control mouse cochlea obtained at 90 DPN. A large gap is highlighted (arrow).

C, C'. An optical section from the center of a similarly stained IHC, from the mid-apical region of a 90 DPN cochlea in which CA-ERBB2 had been activated. Gaps in MYO7 (C, green) and MAP2 (C', red) are also evident.

D, D'. An optical section from the center of a similarly stained IHC, from the mid-basal region of a 90 DPN cochlea in which CA-ERBB2 had been activated. A large gap in cytoplasmic staining is highlighted (arrow). Images were chosen to illustrate gaps in specific places in IHCs from 3 biological replicates of each genotype.